International Journal of Heat and Mass Transfer 111 (2017) 1218–1233

Contents lists available at ScienceDirect

International Journal of Heat and Mass Transfer

journal homepage: www.elsevier.com/locate/ijhmt

Analytical and experimental determination of slug flow parameters, pressure drop and heat transfer coefficient in micro-channel condensation

Gangtao Liang [a,b], Nikhin Mascarenhas [b], Issam Mudawar [b,*]

[a] Key Laboratory of Ocean Energy Utilization and Energy Conservation of Ministry of Education, School of Energy and Power Engineering, Dalian University of Technology, Dalian 116024, China

[b] Purdue University Boiling and Two-Phase Flow Laboratory (PU-BTPFL), School of Mechanical Engineering, 585 Purdue Mall, West Lafayette, IN 47907, USA

ARTICLE INFO

Article history:
Received 1 February 2017
Received in revised form 3 April 2017
Accepted 10 April 2017
Available online 28 April 2017

Keywords:
Micro-channel
Condensation
Slug flow
Hydrodynamic instability

ABSTRACT

This paper investigates slug flow associated with condensation along a module containing 10 of 29.9-cm long micro-channels having 1 × 1-mm^2 cross section. Using FC-72 as condensing fluid, which is cooled by water counterflow, experiments are performed to measure pressure drop as well as detailed temperature variations along the condensation module. Using high speed video, the flow is shown to consist of a series of unit cells, each comprised of a liquid slug and an elongated bubble. New interfacial instability theory is developed to describe the transition from annular flow to slug flow and obtain analytical expressions for bubble and slug lengths for the most upstream unit cell. Also presented is a new theoretical model for slug flow that is used to determine axial variations of bubble, slug and unit cell lengths. These lengths are used to evaluate axial variations of the local heat transfer coefficient, which are accurately predicted using the new model. Additionally, pressure drop data show good agreement with predictions of a recent universal correlation approach for condensation in small channels.

1. Introduction

1.1. Adaptation of micro-channel condensers in thermal management systems

Pursuit of superior performance in many advanced technologies is becoming increasingly a function of the ability to remove large amounts of heat from very small devices. Examples include computer data centers, hybrid vehicle power electronics, avionics, lasers, and radars [1,2]. Despite their relative ease of implementation, single-phase liquid cooling solutions are being abandoned in favor of their two-phase counterparts because of limitations arising from the relatively low heat transfer coefficients attainable with single-phase cooling. Two-phase solutions provide far more superior performance by capitalizing upon both sensible and latent heat of the coolant, resulting in orders of magnitude enhancement in heat transfer coefficients.

A complete two-phase thermal solution must tackle three important functions, removing the heat by flow boiling or evaporation, transmitting the heat using an appropriately sized two-phase flow loop, and rejecting the heat to the ambient via a condenser. The quest for compact and lightweight cooling solutions has spurred significant interest in recent years in the development of miniature boilers utilizing micro-channel heat sinks [2]. Most initial developments were based on the assumption that the heat rejection could be easily managed with the aid of a conventional air-cooled condenser. However, there is now growing interest in developing two-phase cooling solutions that utilize separate cooling loops [3,4]: a primary cooling loop that contains both the miniature boiler and a miniature condenser, and a secondary cooling loop that extracts the heat from the primary loop's condenser and rejects it to ambient air using a remote, conventional air-cooled condenser. The same micro-channel heat sink technology adopted in the miniature boiler can be incorporated in the miniature condenser of the primary loop. Despite their high cooling potential, micro-channel condensers have received far less attention than micro-channel boilers. The present study is focused on the pressure drop and heat transfer characteristics of micro-channel condensers.

* Corresponding author.
E-mail address: mudawar@ecn.purdue.edu (I. Mudawar).
URL: https://engineering.purdue.edu/BTPFL (I. Mudawar).

http://dx.doi.org/10.1016/j.ijheatmasstransfer.2017.04.045
0017-9310/

Nomenclature

A	micro-channel cross-sectional area
A_k	coefficient in potential function relation for phase k in instability model
C	empirical constant used to define frictional pressure gradient multiplier
c	wave speed
Ca	Capillary number
C_c	contraction factor
c_p	specific heat at constant pressure
D	diameter
D_h	hydraulic diameter
f	friction factor
G	mass velocity
H	layer height
h	heat transfer coefficient
H_b	distance between copper block's thermocouple planes
h_{fg}	latent heat of vaporization
H_t	distance between top thermocouple plane and base of micro-channel
k	wave number; thermal conductivity
k_c	critical wave number
L	length
$\dot{m}$	mass flow rate
N	number of micro-channels
P	micro-channel perimeter
p	pressure
Δp	pressure drop
P_e	input power to pre-heater
Q	volume flow rate
q''	heat flux
q''_b	channel bottom wall heat flux
Re	Reynolds number
Su	Suratman number
T	temperature
t	time
T^*	thermodynamic equilibrium temperature
U	mean velocity
u	velocity in z-direction
v	velocity in y-direction
$V_{i,n}$	normal component of interface velocity
v_{fg}	specific volume difference between saturated vapor and saturated liquid
W	width of copper block
W_{ch}	width (and height) of square micro-channel
W_s	width of solid wall separating micro-channels
X	Lockhart-Martinelli parameter
x	vapor quality
x_e	thermodynamic equilibrium quality
y	coordinate defined in Fig. 6(a)
z	axial coordinate

Greek symbols

α	void fraction
β	channel aspect ratio
Γ	dimensionless heat transfer parameter in instability model
δ	film thickness in slug flow regime
δ^+	film thickness in annular flow regime
η	perturbation height in interfacial instability model
η_0	perturbation amplitude in interfacial instability model
λ_c	critical wavelength
μ	viscosity
ρ	density
ρ^+	modified density
σ	surface tension
σ_c	area ratio, $A/(W_pH_p)$
τ	period of bubble generation
ϕ	velocity potential in instability model

Subscripts

A	acceleration
a	average
b	bubble
c	cell; critical; contraction
ch	channel
e	expansion
exp	experimental (measured)
F	frictional
f	film; liquid
fo	liquid only
g	vapor
go	vapor only
h	homogeneous
i	imaginary component; interface
in	inlet
k	phase, $k = g$ or f
out	outlet
p	plenum
pre	pre-heater
$pred$	predicted
r	real component
s	liquid slug
sat	saturation
sp	single phase
tp	two-phase
w	water

1.2. Pressure drop and flow regimes in condensing flows

Even though pressure drop is fairly predictable for single-phase micro-channels using both computational models and empirical correlations [5], it is far more illusive for two-phase micro-channels. Two-phase pressure drop in micro-channels consists of frictional, acceleration (or deceleration), and gravitational components; the latter is negligible for most micro-channel devices. Acceleration is encountered in boiling flows because of a streamwise decrease in two-phase mixture density, while condensing flows are associated with flow deceleration because of an axial increase in mixture density. And, while acceleration increases pressure drop for boiling flows, deceleration decreases pressure drop in condensing flows.

Pressure drop in condensing flows is also influenced by the two-phase flow regime or regimes prevalent along the condensing channel. The condensation flow regimes are generally classified into pure vapor, annular, slug, bubbly, and pure liquid [6,7]. The annular flow regime is established in the upstream region of the channel once vapor begins to condense into a liquid film along the inner channel walls. The film is typically very thin and shear driven by the faster-moving central vapor core. Interfacial instability between the vapor core and liquid film promotes the formation of interfacial waves that grow in amplitude along the channel. Eventually, wave crests from opposite sides of the channel begin to merge, triggering a transition to slug flow. As more of the vapor condenses to liquid in the slug flow regime, the length of liquid slugs increases while that of the oblong bubbles decreases. Bubbly

flow commences once the length of the slug flow bubble decreases to the size of the channel. Ultimately, all vapor bubbles condense and the flow is converted to pure liquid.

Of the different condensation regimes, the annular regime has received the most attention because the thin annular film enables this regime to deliver the highest heat transfer coefficients, let alone the prevalence of annular flow over the largest fraction of the channel length for most practical condenser designs. The clear separation between the liquid and vapor renders the annular regime especially attractive for theoretical modeling. This is accomplished by applying conservation relations separately to the liquid film and vapor core, and employing appropriate boundary conditions along the interface [6–8]. Despite this theoretical appeal, predictions of annular flow are based mostly on empirical formulations [9–12].

1.3. Slug flow regime in condensing micro-channel flows

Although the annular regime is most prevalent, the portion of the channel length incurring slug flow can have an appreciable influence on condensation pressure drop and heat transfer at high coolant mass velocities. Being an intermittent flow regime, slug flow is far more difficult to model, which explains the very limited number of published studies addressing modeling of this regime. In the slug flow regime, the flow fluctuates between regions of high vapor quality and those of virtually zero quality, and the frequency and axial span of the fluctuations vary along the channel due to condensation. Associated with these fluctuation are corresponding fluctuations in bubble length and liquid velocity, which have profound influences on both pressure drop and heat transfer, and which cannot be accurately captured using popular models or correlations based on annular flow assumptions.

A fewer number of studies have been published that address slug flow in small channels. Zhang et al. [13] presented flow visualization results for slug flow of nitrogen-water mixtures in horizontal circular micro-channels with inner diameters from 302 to 916 μm. Odaymet and Louahlia-Gualous [14] discussed slug flow formation in water flow condensing along a square microchannel with a hydraulic diameter of 350 μm. Kim et al. [6,7] provided flow visualization results for condensation of FC-72 through multiple, parallel, 1-mm square channels, which included annular, wavy-annular, slug and bubble regimes, and recommended empirical methods to determine the transitions between regimes. Comparing photos of slug flow bubbles from these three studies reveals distinct differences in the shape of the bubble tail, which can be attributed to the drastic differences in thermophysical properties of the fluids used, especially surface tension.

1.4. Slug flow models

Models for slug flow have been proposed in a few studies. Dukler and Hubbard [15] examined gas-liquid flow in a 38-mm diameter horizontal tube and proposed that pressure drop within the bubble portions of the tube is negligible, *i.e.*, the pressure drop is dictated entirely by the liquid slugs between the bubbles. They employed a logarithmic turbulent velocity profile in the liquid slug to develop an analytical pressure drop model. Nicholson et al. [16] also investigated pressure drop in slug flow and arrived at a model for relatively large diameter horizontal tubes. Fukano et al. [17] investigated air-water slug flow through horizontal tubes with diameters ranging from 1.0 to 4.9 mm, and used their flow visualization results and pressure drop data to construct a pressure drop model for slug flow. Like Dukler and Hubbard, Fukano et al. neglected pressure drop contributions of the bubbles, but suggested that pressure drop is strongly influenced by liquid flow from the annular liquid film of the bubble to the downstream liquid slug. They correlated the slug length in terms of superficial velocities of the two phases and showed that the ratio of bubble velocity to liquid slug velocity is about 1.2 regardless of operating conditions. This velocity ratio is consistent with a value recommended in a much earlier study by Suo and Griffith [18], who also neglected pressure drop contributions of the bubbles. Taitel and Barnea [19] developed a closed-form coupled numerical expression for film thickness and pressure drop for slug flow in relatively large diameter channels. Chung and Kawaji [20] proposed a model based on the assumptions of constant slug length and uniform film thickness, describing the flow as consisting of unit cells whose number was evaluated from a void fraction database for nitrogen-water flow in 50–530-μm channels.

1.5. Objectives of study

This study provides an experimental and theoretical treatment of slug flow associated with condensation of FC-72 along parallel, square 1-mm channels. First, the true vapor quality is extrapolated from thermodynamic quality using an exponential decay function. Second, a new hydrodynamic instability model is developed to determine the initial lengths of slugs and bubbles, variations of which along the stream-wise direction are then determined by applying an energy balance to each unit cell. Pressure drop is predicted using a recent universal approach for condensation in mini/micro-channels. Also presented is a technique to predict the local heat transfer coefficient based on variations of slug parameters along the channel length.

2. Experimental methods

2.1. Fluid conditioning system

Fig. 1(a) shows a schematic diagram of the experimental apparatus used in this study. The apparatus consists of two flow loops, a primary loop for conditioning the condensing fluid, FC-72, and a secondary water cooling loop. Heat is exchanged between the two loops in the system's main condensation test module as well as in a second plate-type heat exchanger.

FC-72 is a dielectric fluid with a moderate boiling point of 56 °C at 1 atmosphere. Both its surface tension and latent heat of vaporization are much smaller than those for water. Table 1 provides thermophysical properties of FC-72 at 57 °C, which is the saturation temperature corresponding to the average operating pressure of the present study.

In the primary flow loop, FC-72 liquid is pumped from a reservoir and passed through one of two flow meters followed by an in-line electric heater, before entering the condensation module as superheated vapor or two-phase mixture with the desired quality. Power input to the FC-72 is regulated with the aid of a variable voltage transformer. To determine the quality at the inlet to the condensation module, the fluid temperature and pressure are measured both at the inlet to the in-line heater and in the condensation module's inlet plenum. Inside the condensation module, the two-phase FC-72 mixture is condensed by rejecting heat to a counter-flow of water from the secondary loop. The FC-72 temperature and pressure are also measured in the condensation module's outlet plenum. Exiting the condensation module, the FC-72 is passed through the plate-type heat exchanger to condense any residual vapor before returning to the primary loop's reservoir in pure liquid state.

The primary component of the water loop is a Lytron modular cooling system consisting of a reservoir, pump, and fan-cooled coiled-tube heat exchanger. Water from the Lytron system is supplied through two parallel branches, one leading to the

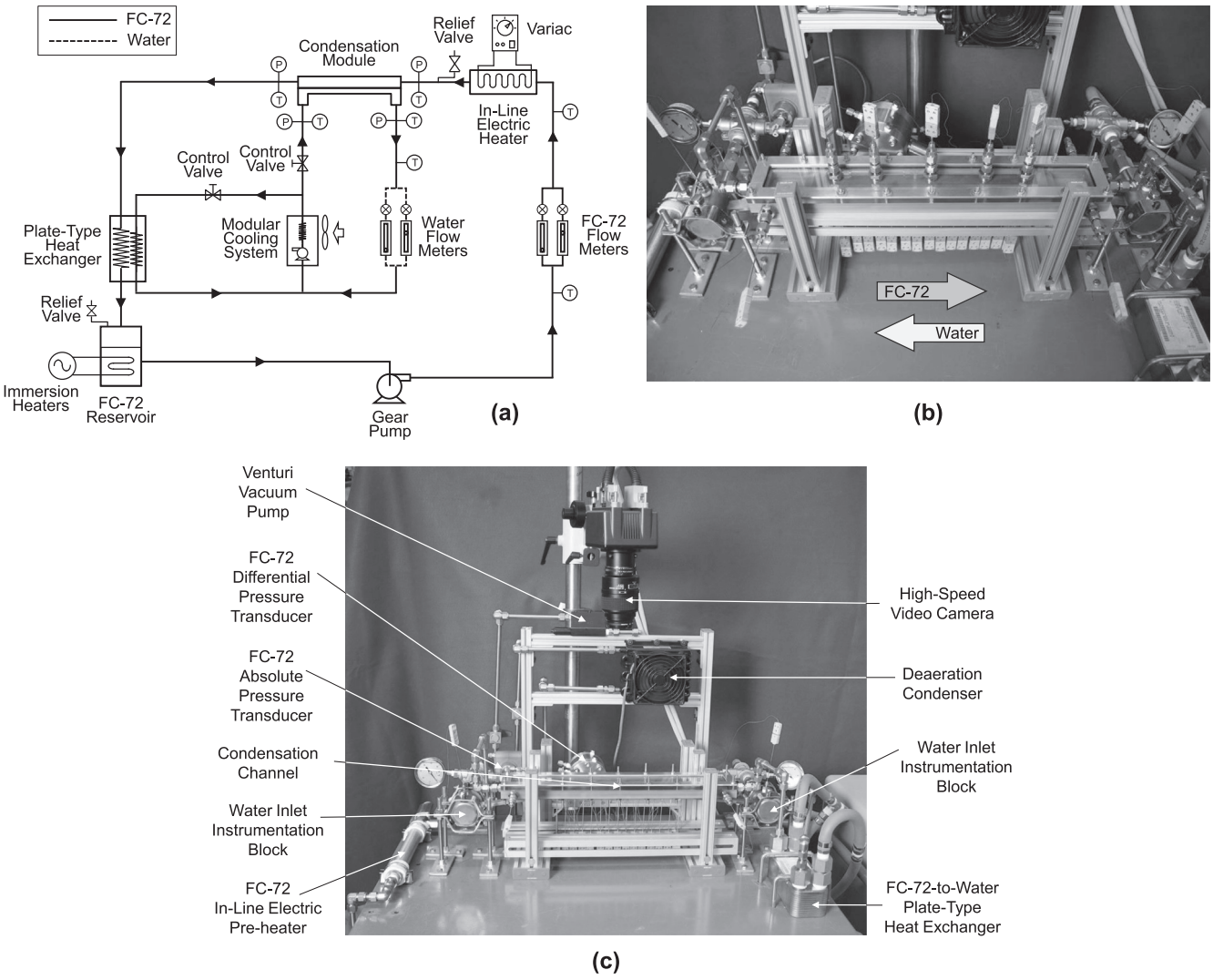

Fig. 1. (a) Schematic diagram of test loop. (b) Photo of micro-channel condensation module. (c) Photo of main part of test apparatus.

Table 1
Thermophysical properties of FC-72 at T_{sat} = 57 °C.

ρ_f [kg/m^3]	ρ_g [kg/m^3]	μ_f [kg/m·s]	k_f [W/m·K]	$c_{p,f}$ [kJ/kg·K]	σ [mN/m]	h_{fg} [kJ/kg]
1591.23	13.56	4.32×10^{-4}	0.0537	1.1026	8.31	94.68

condensation module and the other to the plate-type heat exchanger. The water warms up as it extracts heat from the FC-72 in both the condensation module and heat exchanger, and is returned to the Lytron system. The water is cooled to near room temperature by an air-cooled heat exchanger internal to the Lytron system.

Fig. 1(b) and (c) show photos of the micro-channel condensation module and main part of the experimental apparatus, respectively.

2.2. Micro-channel condensation module

Fig. 2(a) and (b) illustrate the construction of the micro-channel condensation module. The module is comprised of a condensation copper block, water channels, insulating housing, and cover plate. The top of the oxygen-free copper block is 2-cm wide by 29.9-cm long and contains 10 of 1×1-mm^2 square FC-72 condensation channels. Made from transparent polycarbonate (Lexan) plastic, the top cover plate forms top surfaces for the channels as well as provides optical access to the condensing flow. The cooling water flows in a direction opposite to that of the FC-72 through three 3.8×3.8-mm^2 brass tubes soldered to the underside of the copper block. Sixteen pairs of type-E thermocouples are embedded in the copper block along two parallel planes below the condensation channels at 19-mm axial intervals. The thermocouple pairs are used to determine the stream-wise distributions of both the heat flux and temperature at the base of the micro-channels. The insulating G-10 housing both encloses and insulates the copper block, as well as provides inlet and outlet plenums for the FC-72 channels containing ports for pressure and temperature measurements. The G-10 housing and water channels are further insulated with several layers of fiberglass. Table 2 provides detailed dimensions of the condensation module.

2.3. Operating conditions

Two primary objectives of the experiments are to measure the pressure drop and heat transfer coefficient for slug flow during condensation along the square channels. This task is complicated by prevalence of multiple flow regimes along the channel, including annular, slug, bubble, and single-phase liquid. Operating condi-

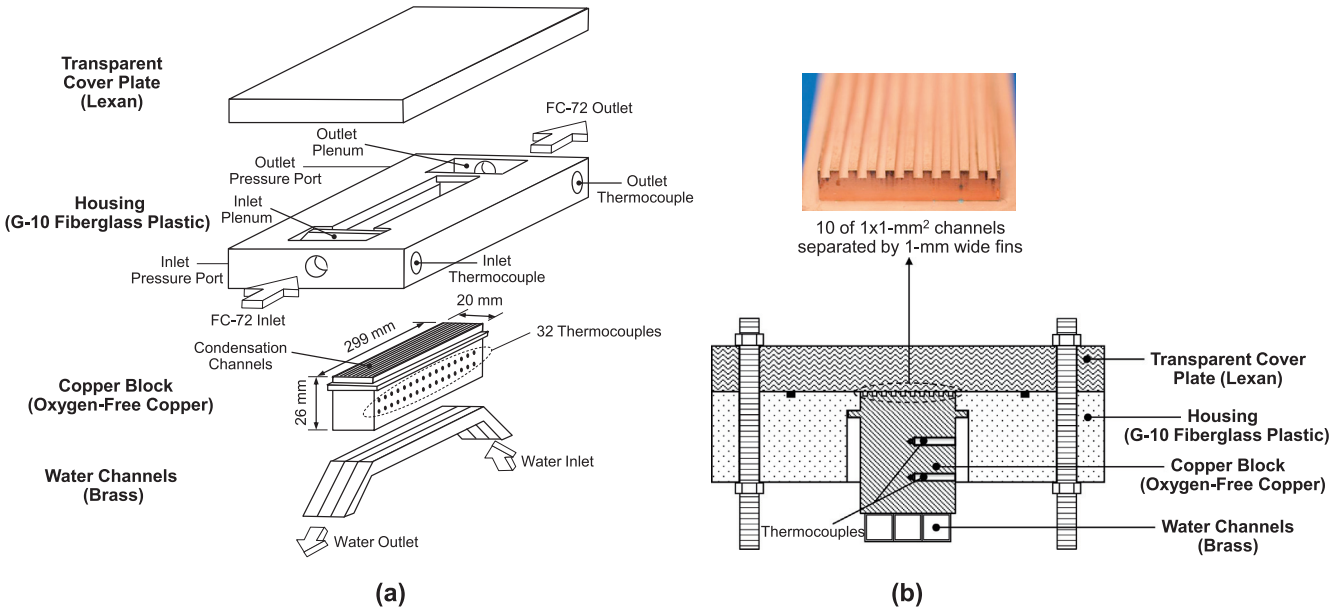

Fig. 2. (a) Construction and (b) cross-sectional view of micro-channel condensation module.

Table 2
Key dimensions of condensation module.

W_{ch} [mm]	H_{ch} [mm]	W_s [mm]	H_t [mm]	H_b [mm]	L [cm]	N
1.0	1.0	1.0	9.65	7.62	29.9	10

tions are therefore sought that yield slug flow over at least 70% of the channel length using different combinations of FC-72 and water flow rates and pre-heater's electrical power input. The FC-72 and water flow rate capabilities of the test apparatus and fixed channel length limit the number of possible tests with predominantly slug flow to nine. Table 3 provides, for each of the nine tests, the mass velocity of FC-72, G, water flow rate, $\dot{m}_w$, thermodynamic equilibrium quality of FC-72 at the module's inlet, $x_{e,in}$, pre-heater's power input, P_e, and axial location corresponding to the onset of slug flow. Inlet plenum pressure is maintained fairly constant at 1.01–1.03 bar for all nine tests. To achieve slug flow very close to the channel inlet, operating conditions are set to achieve an inlet quality close to unity. Table 3 shows that the FC-72 is introduced to the condensation module with a thermodynamic equilibrium quality of $x_{e,in} = 0.908–1.262$. Notice that, by increasing G, maintaining slug flow requires a simultaneous increase of $\dot{m}_w$. However, there are several constraints to achieving slug flow. For example, a large increase in $\dot{m}_w$ causes a large axial decrease in quality, resulting in single-phase liquid flow over an appreciable fraction of the channel length. A broad single-phase liquid region will also be achieved when employing very low G values even when using very low $\dot{m}_w$. Slug flow size measurements are achieved with the aid of a high-speed video motion analysis system. Two key requirements for capturing interfacial features with high resolution are high shutter speed and high magnification. These goals are achieved with the aid of a Photron FASTCAM-Ultima camera capable of shutter speed up to 1/120,000 s, which is used in conjunction with an assortment of Infinity K-2 close-up lenses.

2.4. Measurement uncertainties

FC-72 pressure is measured in the inlet plenum of the condensation module with the aid of an absolute pressure transducer, while a differential pressure transducer measures pressure drop between the inlet and outlet plenums. Temperatures in the inlet and outlet plenums, copper block, inlet to the in-line heater, and in the water channels are measured by type-E thermocouples. All measurements are made after the system pressures and temperatures reach steady state.

Measurement uncertainties of the pressure transducers and flow meters are estimated at ±0.5% and ±2.0%, respectively. The thermocouples embedded in the copper block are carefully

Table 3
Test matrix.

Test No.	Mass velocity of FC-72, G [kg/m² s]	Water flow rate, $\dot{m}_w$ [g/s]	Channel inlet quality, $x_{e,in}$	Pre-heater power input, P_e [W]	Axial location for onset of slug flow [cm]	Film thickness in annular regime, δ^+ [mm]
1	61.63	5.46	0.908	101.1	7.8	0.083
2	61.63	4.56	0.908	100.9	8.2	0.083
3	46.25	4.56	0.965	81.9	5.0	0.052
4	46.25	3.53	0.965	85.5	6.0	0.063
5	46.25	2.54	0.965	86.5	7.0	0.073
6	31.25	4.56	1.262	76.2	2.8	0.029
7	31.25	3.53	1.262	76.4	3.0	0.023
8	31.25	2.54	1.262	76.5	3.2	0.026
9	31.25	1.58	1.262	76.6	4.5	0.032

calibrated using a procedure described in detail by Kim et al. [6] using the same apparatus as the present study. This procedure brings down thermocouple uncertainty to less than ±0.03 °C, and this offset is corrected for individual thermocouples by the data acquisition system. By using five thermocouple ports attached to the top of the cover plate, heat loss through the cover plate is estimated to be less than 2% of the heat input through the base of the micro-channels, which is calculated using the assumption of one-dimensional heat conduction between the two thermocouple planes.

The highest measurement uncertainties are encountered at the lowest FC-72 mass velocity of $G = 31.25\ kg/m^2\ s$, which are estimated at 8.72%, 9.02%, and 13.09% for base heat flux, vapor quality, and heat transfer coefficient, respectively.

3. Experimental results

3.1. Flow visualization results

Fig. 3(a) depicts, for each of the nine tests, video images and corresponding schematics, respectively, of slug flow at the axial location of slug flow initiation. This is defined as the location where the first clearly identifiable slug flow bubble is observed. The images are shown for only two representative neighboring channels. The location of slug flow initiation is significant in that it marks measurable changes in the pressure drop and heat transfer characteristics compared to annular flow. As indicated in Table 3, slug flow is initiated farther upstream for low G values, which is consistent with the flow regime maps of Kim et al. [6]. The first identifiable slug flow bubble has nearly the same length (4.5–4.9 mm) for all test cases, while the length of the liquid slug between bubbles at the same location ranges from 1 to 3 mm. The bubbles are symmetrical and hemispherical at both the front and tail. The liquid film is extremely thin around the perimeter of the bubble, excepting near the front and tail, where the film merges with the upstream and downstream liquid slugs, respectively. Unlike common macro flow depictions of slug flow, no small bubbles are entrained in the liquid slugs.

Fig. 3(b) shows corresponding images and schematics for the channel exit. Here, bubbles are shown for three channels to better capture infrequent bubble formations. Notice that the bubbles at this location for all test cases approach spherical shape, rather than the typical oblong shape of slug flow. Overall, the flow pattern gradually transitions from slug flow to bubbly flow at the channel exit, but the latter occupies only a very small fraction of the channel length.

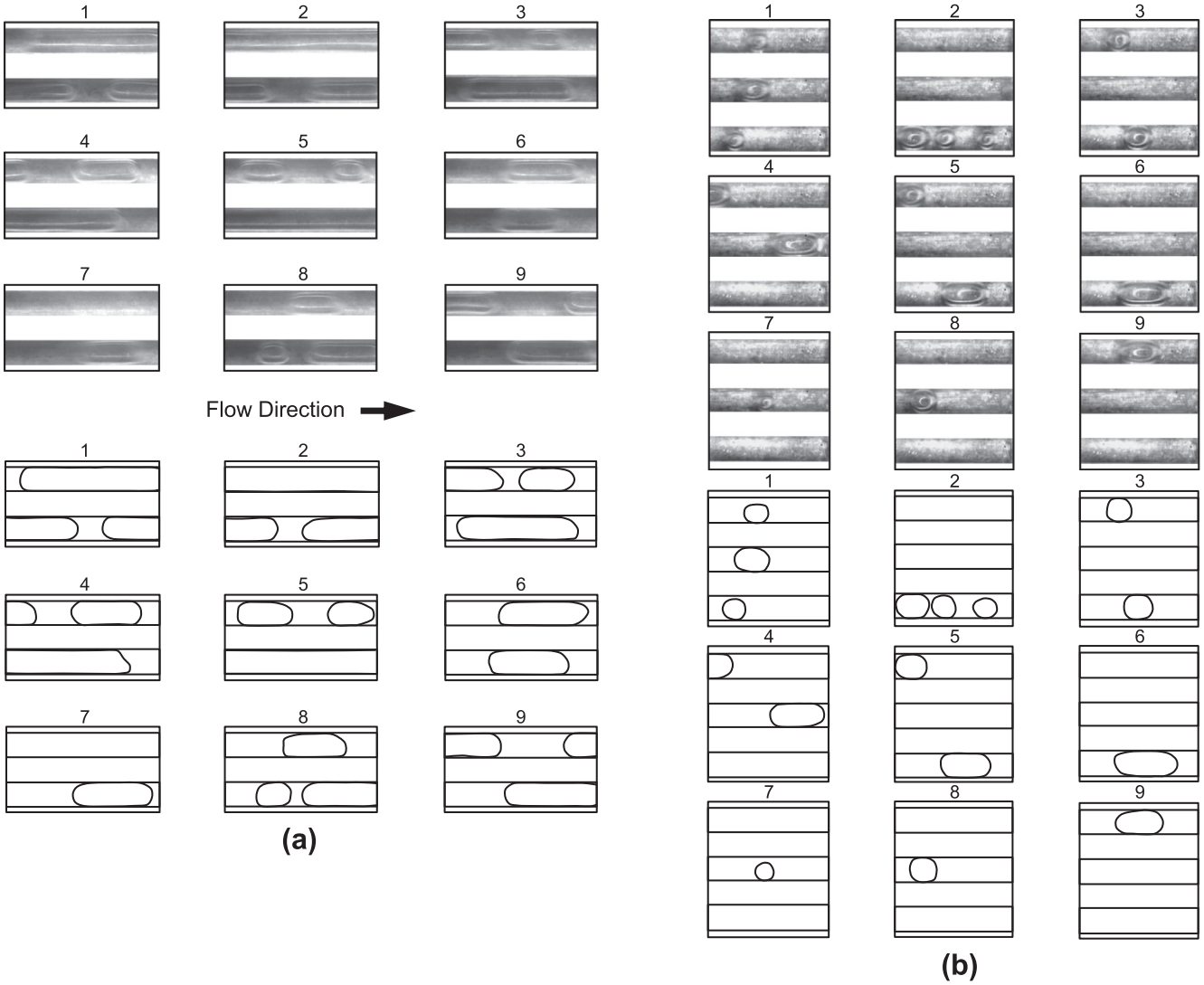

Fig. 3. Images and corresponding schematics of slug flow for the nine test cases at (a) axial location of slug flow initiation, and (b) channel exit.

3.2. Local heat flux and quality

The 16 thermocouple pairs embedded in the copper block are used to measure the temperature gradient along the length of the micro-channel. Both local heat flux, q''_b, and temperature along the base plane of the channels are evaluated using the assumption of one-dimensional heat conduction between the two thermocouple planes. Fig. 4(a) shows, for Test 1 (see Table 3), the temperatures measured along the lower and upper thermocouple planes, along with the extrapolated channel bottom wall temperatures. Fig. 4(b) shows the axial heat flux variations for all nine tests.

FC-72 enters the pre-heater situated upstream of the condensation module in subcooled liquid state at temperature T_{pre}, and is brought to near-saturated or superheated vapor state by the pre-heater's electrical power input, P_e. Thermodynamic equilibrium quality at the inlet to the condensation module is obtained by applying energy balance to the pre-heater,

$$x_{e,in} = -\frac{c_{p,f}(T_{sat,pre} - T_{pre})}{h_{fg,pre}} + \frac{P_e}{\dot{m}\, h_{fg,pre}}. \tag{1}$$

Variation of thermodynamic equilibrium quality along the channel is obtained by applying a differential energy balance along the micro-channel length,

$$x_e(z + \Delta z) = x_e(z) - \frac{W}{\dot{m}\, h_{fg}}\left[\frac{q''_b(z + \Delta z) + q''_b(z)}{2}\right]\Delta z, \tag{2}$$

where W is the width of the copper block at the base of the channels.

As will be shown below, Eq. (2) provides thermodynamic equilibrium quality values that fall below zero at some axial distance along the channel for all the 9 tests where slug flow is observed over a large fraction of the channel length. This is indicative of appreciable non-equilibrium effects prevailing along the channel, which is common to many two-phase flows with heat transfer. Therefore, the thermodynamic equilibrium quality does not provide an accurate measure of vapor content that can be used to determine slug flow parameters. A more representative measure of quality is therefore needed that maintains the observed positive value where x_e falls below zero. The approach adopted here is to devise an appropriate measure of vapor quality in pursuit of a useful expression for void fraction, α.

In his model of subcooled flow boiling, Levy [21] recommended a relationship between 'true quality', x, and thermodynamic equilibrium quality, x_e, using an exponential decay function for the upstream subcooled flow boiling region. A similar approach is adopted in the present study for the downstream subcooled condensation region using the expression

$$x = x_e + \frac{c_{p,f}(T_{sat} - T_f)}{h_{fg}} \exp\left\{\frac{x_e h_{fg}}{c_{p,f}(T_{sat} - T_f)} - 1\right\}, \tag{3}$$

where T_f^* is the calculated thermodynamic equilibrium temperature of liquid FC-72 at the downstream axial location where the bubble length just falls below the channel width, W_{ch}, since this location marks where very rapid collapse of vapor to near zero quality takes place. Fig. 5(a) shows the variations of x_e and x along the channel for Test 1. Notice how Eq. (3) provides physically correct values for quality, whereas x_e shows non-equilibrium negative values. Fig. 5 (b) shows the axial variations of x for all 9 test cases.

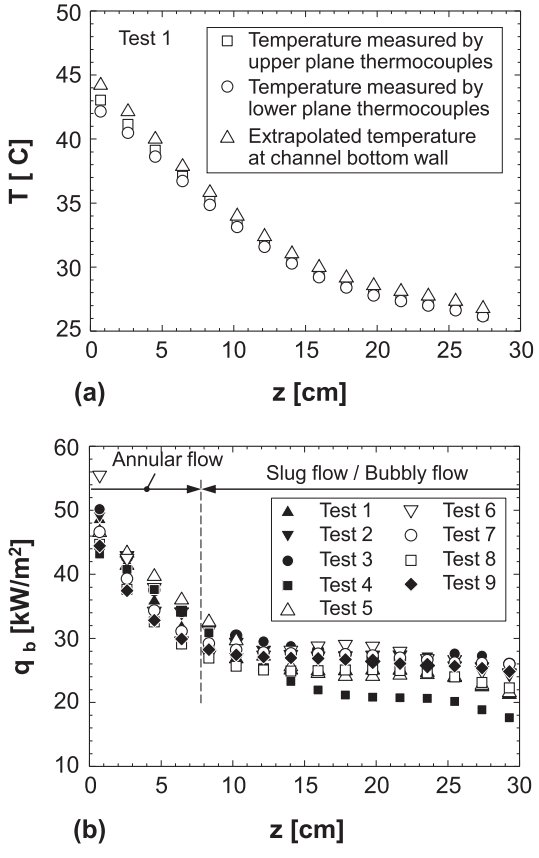

Fig. 4. (a) Axial variations of copper block thermocouple temperatures and calculated channel bottom wall temperatures for Test 1. (b) Axial variations of channel bottom wall heat flux for all nine tests.

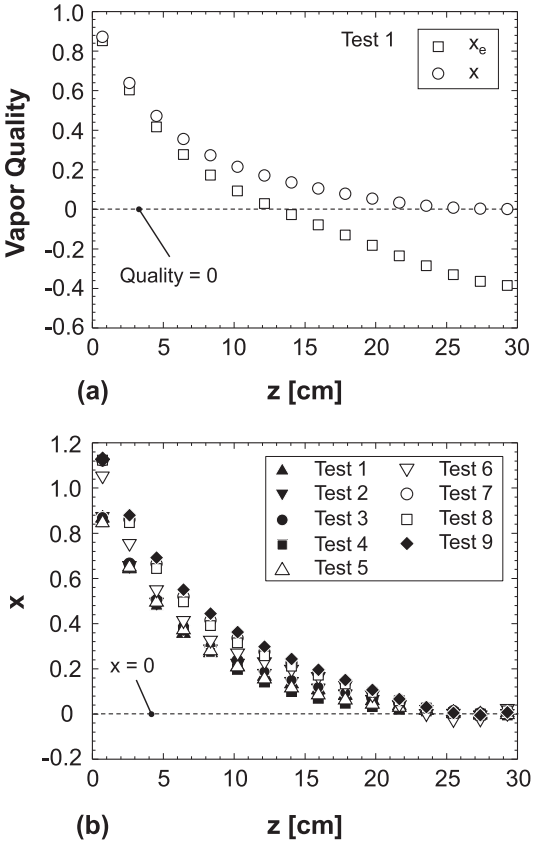

Fig. 5. (a) Axial variations of quality, x, and thermodynamic equilibrium quality, x_e, for Test 1. (b) Axial variations of quality, x, for all nine tests.

4. Model for interfacial instability with heat transfer

The hydrodynamic instability theory depicted in Fig. 6(a) has been successfully used in the past to predict a variety of transitional characteristics in two-phase flow. These include critical heat flux in both pool boiling [22,23] and flow boiling [24–27]. This theory has also been used to determine the flow conditions that result in transition from annular flow to slug flow [28–30]. This transition is described to occur when waves along the annular film's interface grow in amplitude until a critical wavelength is reached, and the wave crests from diametrically opposite parts of the channel begin to merge. The critical wavelength is analytically modeled in terms of dimensionless groups that account for mean velocities and densities of the liquid and vapor, channel diameter, film thickness, and surface tension.

In the present study, hydrodynamic instability theory is extended to predict the size of slug flow bubbles and liquid slugs in the presence of heat transfer at the wall. Summarized in Appendix A is the classical instability model for this configuration [27,31–32], which is followed below by a new instability model that accounts for heat transfer across the interface.

The influence of heat flux due to condensation can be incorporated into the instability analysis via heat fluxes q_g'' and q_f'' on the vapor and liquid sides, respectively, of the interface as shown in Fig. 6(b). These heat fluxes alter the normal stress balance given by Eq. (A7). To incorporate the heat transfer effects, the interfacial mass, momentum, and energy interfacial conditions are modified into

$$\rho_g\left(\frac{\partial\phi_g}{\partial y}-V_{i,n}\right)=\rho_f\left(\frac{\partial\phi_f}{\partial y}-V_{i,n}\right), \tag{4a}$$

$$\left[p_g+\rho_g\left(\frac{\partial\phi_g}{\partial y}-V_{i,n}\right)\frac{\partial\phi_g}{\partial y}\right]-\left[p_f+\rho_f\left(\frac{\partial\phi_f}{\partial y}-V_{i,n}\right)\frac{\partial\phi_f}{\partial y}\right]=\sigma, \tag{4b}$$

and

$$q_g''-q_f''=\rho_f\left(\frac{\partial\phi_f}{\partial y}-V_{i,n}\right)h_{fg}, \tag{4c}$$

respectively, where $V_{i,n}$ is the normal component of the interface velocity.

Combining Eqs. (4a)–(4c) gives

$$p_g-p_f+\left(\frac{q_g''-q_f''}{h_{fg}}\right)\left(\frac{\partial\phi_g}{\partial y}-\frac{\partial\phi_f}{\partial y}\right)=\sigma\frac{\partial^2\eta}{\partial z^2}, \tag{5}$$

and Eq. (A13) is modified into

$$iA_g\left[\rho_g(U_g-c)\cosh(kH_g)-i\left(\frac{q_g''-q_f''}{h_{fg}}\right)\sinh(kH_g)\right]-iA_f\left[\rho_f(U_f-c)\cosh(kH_f)+i\left(\frac{q_g''-q_f''}{h_{fg}}\right)\sinh(kH_f)\right]=\sigma\eta_0 k. \tag{6}$$

Substituting Eqs. (A6a) and (A6b) into Eq. (6) gives

$$\left[\rho_g^+(U_g-c)^2-i\left(\frac{q_g''-q_f''}{h_{fg}}\right)(U_g-c)\right]+\left[\rho_f^+(U_f-c)^2+i\left(\frac{q_g''-q_f''}{h_{fg}}\right)(U_f-c)\right]=\sigma k. \tag{7}$$

where $\rho_g^+=\rho_g\coth(kH_g)$ and $\rho_f^+=\rho_f\coth(kH_f)$. Like Eq. (A14), the solution to Eq. (7) can be presented as $c=c_r+ic_i$, where c_r and c_i are given, respectively, by

$$c_r=\left[\frac{\rho_g^+U_g+\rho_f^+U_f}{\rho_g^++\rho_f^+}\right]+\frac{1}{\sqrt{2}}\times\frac{\Gamma}{\left(1+\sqrt{1+\Gamma^2}\right)^{1/2}}\left[\frac{\rho_g^+\rho_f^+(U_g-U_f)^2}{\left(\rho_g^++\rho_f^+\right)^2}-\frac{\sigma k}{\rho_g^++\rho_f^+}\right]^{1/2} \tag{8a}$$

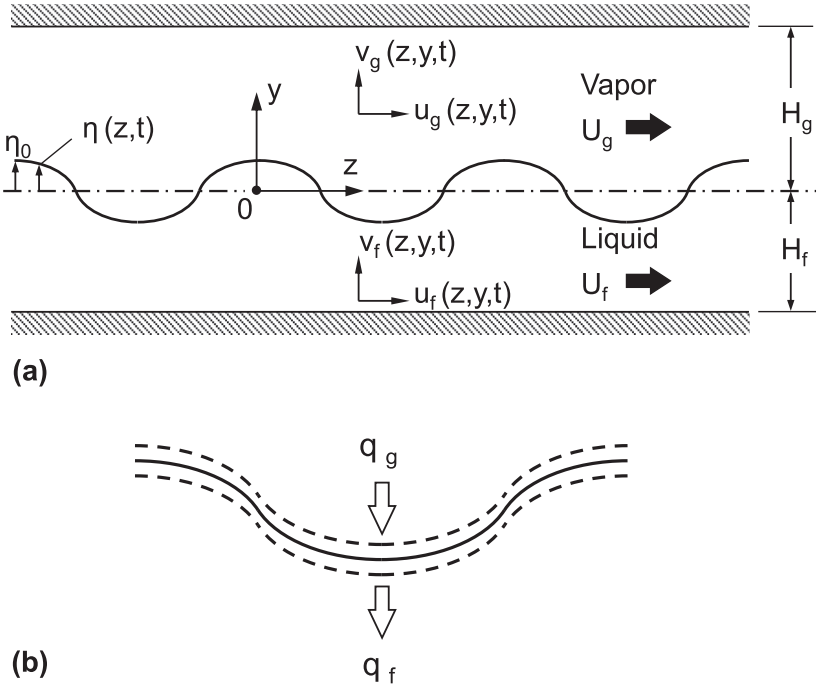

Fig. 6. (a) Hydrodynamic instability between adiabatic gas and liquid layers confined between two infinite parallel solid walls. (b) Vapor and liquid heat fluxes across perturbed interface for new instability model in presence of heat transfer.

and

$$c_i = \left(\frac{1+\sqrt{1+\Gamma^2}}{2}\right)^{1/2}\left[\frac{\rho_g^+\rho_f^+(U_g-U_f)^2}{(\rho_g^+ + \rho_f^+)^2} - \frac{\sigma k}{\rho_g^+ + \rho_f^+}\right]^{1/2}, \tag{8b}$$

where

$$\Gamma = \frac{\left(\frac{q_g''-q_f''}{h_{fg}}\right)\left(\frac{U_g-U_f}{\rho_g^+ + \rho_f^+}\right)}{\left[\frac{\rho_g^+\rho_f^+(U_g-U_f)^2}{(\rho_g^+ + \rho_f^+)^2} - \frac{\sigma k}{\rho_g^+ + \rho_f^+}\right]}. \tag{9}$$

5. Slug flow model

5.1. Model assumptions

Depicted in Fig. 7(a) is a schematic of unit cell evolution in the stream-wise direction, with each unit cell consisting of a liquid slug and an oblong vapor bubble. Fig. 7(a) also provides nomenclature used in the development of the slug flow model. It is assumed that slug flow is initiated by hydrodynamic instability of the annular film in the upstream annular flow regime, and this instability generates the liquid slugs, with oblong vapor bubbles in between, in a periodic manner. Vapor condensation leads to a stream-wise decrease in bubble length and increase in liquid slug length. The slug flow regime terminates downstream, where bubble width becomes smaller than the channel width, and is replaced by bubbly flow.

Before presenting details of the slug flow model, it is crucial to describe the liquid film distribution along the channel's perimeter, given the significant impact this distribution has on both momentum and heat transfer. Bubble shape is dictated mostly by the magnitude of capillary number, which is defined as

$$Ca = \frac{\mu_f U_b}{\sigma}, \tag{10}$$

where, as shown in Fig. 7(a), U_b represents the bubble velocity. Fig. 7(b) contrasts liquid film distribution in a square micro-channel for two ranges of Ca. For $Ca \leq 0.04$, the bubble acquires nearly square shape, while it maintains circular shape for $Ca > 0.04$ [33,34], though a higher transitional value of $Ca = 0.1$ has also been suggested [35,36]. As will be shown later, square bubble shape is maintained for all conditions of the present study. Aside from this assumption, the slug flow model is based on the following simplifying assumptions:

(1) Condensing flow inside the micro-channels is steady, incompressible, and concurrent.
(2) Gravitational effects are negligible.
(3) There are no entrained bubbles inside the liquid slugs, or droplets inside the oblong bubbles.
(4) Thermophysical properties are based on local saturation pressure.

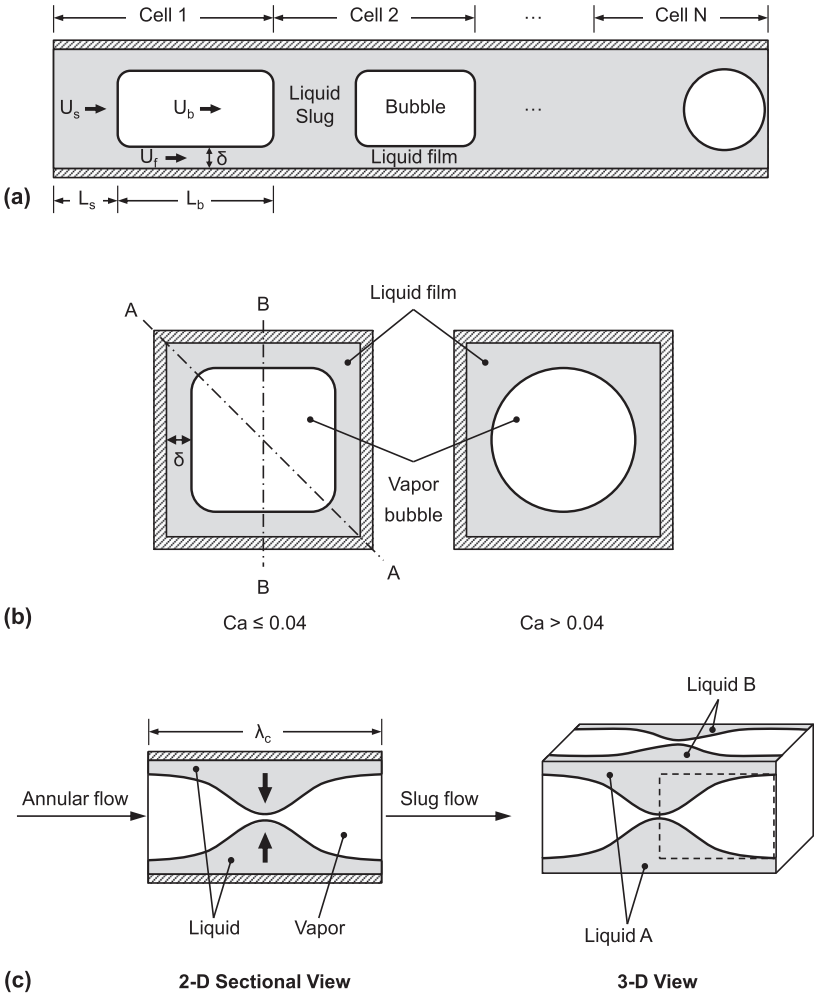

Fig. 7. Schematics of (a) slug flow along the channel, (b) liquid film distribution inside the square micro-channel, and (c) transition from upstream annular flow to slug flow.

(5) Condensation occurs only at the interface between the oblong vapor bubbles and surrounding liquid film.
(6) Heat transfer in the axial direction is negligible.
(7) The liquid film is laminar and has a smooth interface.
(8) Initial film thickness in a unit cell remains constant.
(9) Velocities of bubble, liquid slug, and liquid film do not change along the channel.
(10) Circumferential heat flux is both uniform and constant in the axial direction.

5.2. Model construction

5.2.1. Determination of parameters from upstream annular flow

In this model, interfacial instability is assumed to play a crucial role in initiating the slug flow regime. Shown in Fig. 7(c) is a schematic of the transition from upstream annular flow to slug flow. Interfacial instability causes interfaces from opposite sides of the square channel to merge together producing liquid slugs separated by elongated bubbles. The critical wavelength of instability in the micro-channel depends on several parameters, including vapor and liquid layer thicknesses and velocities, and heat flux. The thicknesses of the vapor and liquid layers are dictated by the upstream annular flow at the axial location corresponding to the onset of slug flow, and therefore given, respectively, by

$$H_f = \delta^+ \tag{11a}$$

and

$$H_g = W_{ch}/2 - \delta^+, \tag{11b}$$

where δ^+ is the film thickness in the annular flow region at the axial location for onset of slug flow. The value of δ^+ is determined using the theoretical model for annular condensation in square micro-channels by Kim and Mudawar [8], and provided in Table 3 for each of the present 9 test cases. The difference in heat flux between the vapor and liquid sides of the interface in the instability model discussed in Section 4 is given by

$$q'' = q''_g - q''_f, \tag{12}$$

where q'' is the heat flux along the channel's heat transfer perimeter. Because cooling in the present study is limited to three sides, q'' can be related to the base heat flux, q''_b, using the relation

$$3W_{ch}\, q'' = (W_{ch} + W_s) q''_b, \tag{13}$$

The vapor and liquid velocities in the upstream annular flow region are given, respectively, by

$$U_g = \frac{G}{\rho_g}\frac{x}{\alpha} \tag{14a}$$

and

$$U_f = \frac{G}{\rho_f}\frac{1-x}{1-\alpha}. \tag{14b}$$

where α is the void fraction in the upstream annular region, which is calculated using Zivi's correlation [37]

$$\alpha = \left[1 + \left(\frac{1-x}{x}\right)\left(\frac{\rho_g}{\rho_f}\right)^{2/3}\right]^{-1}. \tag{15}$$

Substituting Eqs. (11a), (11b), (12), (14a), and (14b) into Eq. (8b), and setting $c_i = 0$ yield the critical wave number k_c, which is used to determine the critical wavelength,

$$\lambda_c = \frac{2\pi}{k_c}. \tag{16}$$

Similar substitutions into Eq. (8a) yield the wave speed, c_r, from which the period of bubble generation in slug flow according to Fig. 7(c) is expressed as

$$\tau = \frac{\lambda_c}{c_r}. \tag{17}$$

5.2.2. Slug flow parameters

To construct a detailed model for slug flow, it is important to derive relations for all key slug flow parameters: bubble velocity, U_b, slug velocity, U_s, film velocity, U_f, film thickness, δ, liquid slug length, L_s, and bubble length, L_b, as shown in Fig. 7(a).

It is important to point out that the interfacial merger depicted in Fig. 7(c) is three dimensional since peaks in the interfacial waves approach the central axis not only from the channel top and bottom walls, but also from the two sidewalls. Liquid within these waves constitutes the first liquid slug, whose initial velocity approaches zero after the merger because liquid film velocity in the annular regime is much smaller than the vapor core velocity. This implies that momentary stagnation of the first liquid slug would compel the upstream vapor flow to decelerate from U_g to zero. It is assumed that the deceleration is uniform, therefore the bubble velocity can be expressed as

$$U_b = 0.5U_g. \tag{18}$$

It is interesting to note that this relation is different from that used in a prior slug flow study, where U_b is assumed to equal U_g [20].

A two-step approach is used to determine the liquid slug velocity, U_s, and liquid film velocity, U_f, in the slug flow regime. The first step is the approximation that U_f is much smaller than U_b and U_s. This is similar to the assumption used by Kreutzer et al. [38], which allows relating U_s to U_b according to

$$\frac{U_b}{U_s} = 1 + \frac{4\delta}{D_h}, \tag{19}$$

where δ is the film thickness in the slug flow regime (see Fig. 7 (a) and (b)), D_h the hydraulic diameter,

$$D_h = \frac{4A}{P}, \tag{20}$$

A ($=W_{ch}^2$) the cross-sectional area of the square channel, and P ($=4W_{ch}$) the channel's wetted perimeter.

To date, investigations of film thickness around bubbles in square micro-channels are quite sparse, and no reliable correlations or models can be found to predict the film thickness. Thulasidas et al. [34] and Kolb and Cerro [35,36] measured film thickness in both the *A-A* and *B-B* planes depicted in Fig. 7(b) using air-water and air-silicone oil slug flows. Their results show that film thickness in the *B-B* direction is virtually independent of *Ca* for $Ca \leq 0.04$, and $\delta/W_{ch} \approx 0.025$. Using a laser focus displacement meter, Han and Shikazono [39] measured film thickness in a square micro-channel, but their correlations are applicable only to bubbles with circular perimeter, and their data showed complex fluctuations of film thickness for small *Ca*. Experiments by Chung and Kawaji [20] involving adiabatic nitrogen-water slug flow showed $\delta/W_{ch} = 0.05$. In the present model, given the weak dependence of initial bubble and slug parameters on δ, the value of δ/W_{ch} is determined from the heat transfer data. For example, values of $\delta/W_{ch} = 0.05$, 0.04, 0.035, 0.03, and 0.025 yielded mean absolute errors in the heat transfer coefficient of 26.1%, 14.3%, 10.2%, 13.6% and 25.5%, respectively, which shows that $\delta/W_{ch} = 0.035$ provides the best predictions. Note that this value is smaller than $\delta/W_{ch} = 0.05$ in Chung and Kawaji, because of the much smaller surface tension of FC-72 compared to that of water.

Shown earlier in Fig. 7(c) is three-dimensional merger of sinusoidal liquid waves during transition from annular to slug flow.

The wave merger occurs between the top and bottom walls (liquid A), as well as between the two sidewalls (liquid B). According to symmetry characteristic of sinusoids, liquid A occupies half of the volume, and liquid B half the volume of liquid A. Therefore, the slug region marked by the dashed rectangle in Fig. 7(c) contains half of the liquid volume, *i.e.*, 3/8th the full volume. Accounting for liquid film thickness δ^+ in the upstream annular region, and δ in the slug region, the volume of the first slug flow bubble can be determined from the relation

$$L_{b1}(W_{ch}-2\delta)^2 = U_b\tau(W_{ch}-2\delta)^2 - \frac{3}{8}\lambda_c(W_{ch}-2\delta^+)^2, \tag{21}$$

which allows bubble length in the first unit cell, L_{b1}, in Fig. 7(a) to be expressed as

$$L_{b1} = U_b\tau - \frac{3}{8}\lambda_c\left(\frac{W_{ch}-2\delta^+}{W_{ch}-2\delta}\right)^2. \tag{22}$$

Also, the volume of liquid that forms the first liquid slug after interfacial merger in the annular regime is given by

$$L_{s1}W_{ch}^2 = \frac{3}{4}\lambda_c(W_{ch}-2\delta^+)^2, \tag{23}$$

where L_{s1} is the initial slug length, which can be expressed as

$$L_{s1} = \frac{3}{4}\lambda_c\left(1-\frac{2\delta^+}{W_{ch}}\right)^2. \tag{24}$$

This equation reveals that the length of the initial slug is determined entirely from parameters of the upstream annular flow region. The total length of the upstream unit cell can therefore be determined from

$$L_{c1} = L_{b1} + L_{s1}. \tag{25}$$

Applying an energy balance to any unit cell yields

$$\frac{dL_s}{dt} = \frac{3}{4}\frac{q''PL_c}{\rho_f A h_{fg}} \tag{26a}$$

and

$$\frac{dL_b}{dt} = -\frac{3}{4}\frac{q''PL_c}{\rho_h A_b h_{fg}}, \tag{26b}$$

where ρ_h, is a homogeneous density which, based on the model assumption that vapor condensation takes place only at the interface between the vapor bubble and liquid film, is expressed as

$$\rho_h = \rho_g\alpha_b + \rho_f(1-\alpha_b), \tag{27}$$

where α_b is the *bubble void fraction* associated with only the bubble portion of the unit cell, and defined as

$$\alpha_b = \frac{(W_{ch}-2\delta)^2}{W_{ch}^2}. \tag{28}$$

This methodology allows the determination of bubble length and slug length at different locations along the stream-wise direction. Because homogeneous density is smaller than that of the liquid, the length of the unit cell will decrease along the channel. This important issue will be discussed later.

5.3. Pressure drop

In this study, total pressure drop is measured between the test section's inlet and outlet plenums. Since test cases are carefully selected where most of the channel length is occupied by slug flow, pressure drop across the micro-channels is associated entirely with two-phase flow. The total pressure drop is expressed as the sum of two-phase pressure drop, ΔP_{tp}, inlet contraction pressure drop, ΔP_c, and outlet expansion pressure drop, ΔP_e,

$$\Delta p = \Delta p_c + \Delta p_{tp} + \Delta p_e, \tag{29}$$

where ΔP_{tp} includes both frictional and acceleration components,

$$\Delta p_{tp} = \Delta p_F + \Delta p_A, \tag{30}$$

Notice that the accelerational component, ΔP_A, is negative for condensing flow due to axial deceleration of the two-phase mixture along the micro-channel.

Following [40], contraction and expansion pressure drops are given, respectively, by

$$\Delta p_c = \frac{G^2}{2\rho_f}\left\{\left(\frac{1}{C_c}-1\right)^2 + (1-\sigma_c^2)\right\}(1+\rho_f x_{e,in}\upsilon_{fg}) \tag{31a}$$

and

$$\Delta p_e = \frac{G^2\sigma_c(\sigma_c-1)}{\rho_f}(1+\rho_f x_{e,out}\upsilon_{fg}), \tag{31b}$$

where σ_c is the ratio of total flow area of micro-channels to flow area of the plenum, and the contraction coefficient, C_c, in Eq. (31a) is given by

$$C_c = 1 - \frac{1-\sigma_c}{2.08(1-\sigma_c)+0.5371}. \tag{32}$$

The acceleration pressure gradient is expressed as [40]

$$-\left(\frac{dp}{dz}\right)_A = G^2\frac{d}{dz}\left[\frac{x^2}{\rho_g\alpha} + \frac{(1-x)^2}{\rho_f(1-\alpha)}\right], \tag{33}$$

where the void fraction, α, is calculated using Eq. (15).

Recently, Kim and Mudawar [40] developed a universal correlation approach to predicting frictional pressure drop in mini/micro-channel flows, which they formulated according to the Lockhart-Martinelli separated flow model [9]. To account for the influence of small channel diameter on pressure drop, the parameter C of the Lockhart-Martinelli model, whose magnitude depends on a combination of four possible vapor and liquid laminar/turbulent flow states, was expressed in terms of liquid-only Reynolds number, Re_{fo}, and vapor-only Suratman number, Su_{go}. This universal approach was based on a consolidated database of 7115 data points for both adiabatic and condensing mini/micro-channel flows amassed from 36 sources. The database is comprised of 17 working fluids (including FC-72), and broad ranges of D_h, G, and x. Table 4 provides the series of equations required to calculate the frictional pressure gradient according to the universal correlation.

5.4. Heat transfer coefficient

It is assumed that thermal conduction through the thin liquid film, expressed in terms of two-phase heat transfer coefficient h_{tp}, dominates heat transfer in each unit cell. A relatively smaller contributor is single-phase heat transfer in the liquid slug region, expressed in terms of single-phase heat transfer coefficient h_{sp}. Therefore, the overall heat transfer coefficient, h, can be expressed as

$$h = h_{sp}\frac{L_s}{L_c} + h_{tp}\frac{L_b}{L_c}. \tag{34}$$

Once the liquid slug passes a given axial location, transient thin-film condensation begins and film thickness begins to increase; the film is thickest at the trailing edge of the vapor bubble. Condensation of vapor across the film along three heat transfer walls (bottom wall and two sidewalls) over a period t corresponding to the onset of passage of the liquid film at the given axial location increases the film thickness from initial value δ_i to δ

Table 4
Universal correlation for predicting frictional pressure drop in condensing mini/micro-channel flows [40].

$\left(\frac{dp}{dz}\right)_F = \left(\frac{dp}{dz}\right)_f \phi_f^2$
where
$\phi_f^2 = 1 + \frac{C}{X} + \frac{1}{X^2}, \quad X^2 = \frac{(dp/dz)_f}{(dp/dz)_g}$
$-\left(\frac{dp}{dz}\right)_f = \frac{2f_f G^2 (1-x)^2}{\rho_f D_h}, \quad -\left(\frac{dp}{dz}\right)_g = \frac{2f_g G^2 x^2}{\rho_g D_h}$
$f_k = 16\, Re_k^{-1}$ for $Re_k < 2000$,
$f_k = 0.079\, Re_k^{-0.25}$ for $2000 \leqslant Re_k < 20,000$,
$f_k = 0.046\, Re_k^{-0.2}$ for $Re_k \geqslant 20,000$,
for laminar flow in a rectangular channel,
$f_k Re_k = 24(1 - 1.3553\,\beta + 1.9467\,\beta^2 - 1.7012\,\beta^3 + 0.9564\,\beta^4 - 0.2537\,\beta^5)$
where subscript k denotes f or g for liquid and vapor phases, respectively,
$Re_f = \frac{G(1-x)D_h}{\mu_f}, \quad Re_g = \frac{GxD_h}{\mu_g}, \quad Re_{fo} = \frac{GD_h}{\mu_f}, \quad Su_{go} = \frac{\rho_g \sigma D_h}{\mu_g^2}$

Liquid	Vapor (gas)	Empirical parameter, C
Turbulent ($Re_f > 2000$)	Turbulent ($Re_g > 2000$)	$C = 0.39\, Re_{fo}^{0.03} Su_{go}^{0.10} \left(\frac{\rho_f}{\rho_g}\right)^{0.35}$
Turbulent ($Re_f > 2000$)	Laminar ($Re_g < 2000$)	$C = 8.7 \times 10^{-4} Re_{fo}^{0.17} Su_{go}^{0.50} \left(\frac{\rho_f}{\rho_g}\right)^{0.14}$
Laminar ($Re_f < 2000$)	Turbulent ($Re_g > 2000$)	$C = 0.0015 Re_{fo}^{0.59} Su_{go}^{0.19} \left(\frac{\rho_f}{\rho_g}\right)^{0.36}$
Laminar ($Re_f < 2000$)	Laminar ($Re_g < 2000$)	$C = 3.5 \times 10^{-5} Re_{fo}^{0.44} Su_{go}^{0.50} \left(\frac{\rho_f}{\rho_g}\right)^{0.48}$

Universal correlation based on consolidated database of 7115 frictional pressure drop data points from 36 sources with the following application ranges:

- Working fluids: air/CO_2/N_2-water mixtures, N_2-ethanol mixture, R12, R22, R134a, R236ea, R245fa, R404A, R410A, R407C, propane, methane, ammonia, CO_2, and water
- Hydraulic diameter: $0.0695 < D_h < 6.22$ mm
- Mass velocity: $4.0 < G < 8528$ kg/m^2 s
- Liquid-only Reynolds number: $3.9 < Re_{fo} = GD_h/\mu_f < 89{,}798$
- Superficial liquid Reynolds number: $0 < Re_f = G(1-x)D_h/\mu_f < 79{,}202$
- Superficial vapor (or gas) Reynolds number: $0 < Re_g = GxD_h/\mu_g < 253{,}810$
- Flow quality: $0 < x < 1$
- Reduced pressure (for 4728 condensing and adiabatic liquid-vapor data): $0.0052 < P_R < 0.91$.

$$\rho_f\, h_{fg}(4\,\delta\, W_{ch}) = \rho_f\, h_{fg}(4\,\delta_i\, W_{ch}) + 3\, q''\, W_{ch}\, t \tag{35a}$$

or

$$\delta = \delta_i + \frac{3}{4}\frac{q'' t}{\rho_f\, h_{fg}}. \tag{35b}$$

Averaging over period τ corresponding to full passage of the liquid film yields the following relation for average film thickness:

$$\delta_a = \frac{1}{\tau}\int_0^{\tau}\left(\delta_i + \frac{3}{4}\frac{q'' t}{\rho_f\, h_{fg}}\right) dt = \delta_i + \frac{3}{8}\frac{q''\tau}{\rho_f\, h_{fg}}. \tag{36}$$

The two-phase heat transfer coefficient can be determined using this average film thickness as recommended by Jacobi and Thome [41],

$$h_{tp} = \frac{k_f}{\delta_a}, \tag{37}$$

In Eq. (34), the single phase heat transfer coefficient associated with the liquid slug is determined from

$$Nu_{sp} = \frac{h_{sp} D_h}{k_f} = 4.36, \tag{38}$$

where the numerical value for Nu_{sp} is obtained from Shah and London [42] for constant heat flux boundary assuming fully developed flow promoted by strong mixing within the liquid slug.

6. Validation of model predictions

Shown in Fig. 8 are values of capillary number, Ca, for all nine test cases, which confirm the assumption made earlier that $Ca \cong 0.04$ for all conditions of the present study, and prove that the bubbles assume a square rather than round cross-section.

Fig. 9(a) presents experimental data of initial bubble length at the location of slug flow initiation, which range from 4.5 to 4.9 mm. Fig. 9(b) shows that measured initial bubble length data

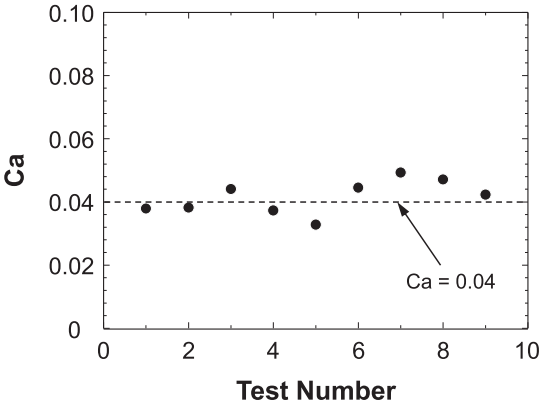

Fig. 8. Capillary number values for nine test cases.

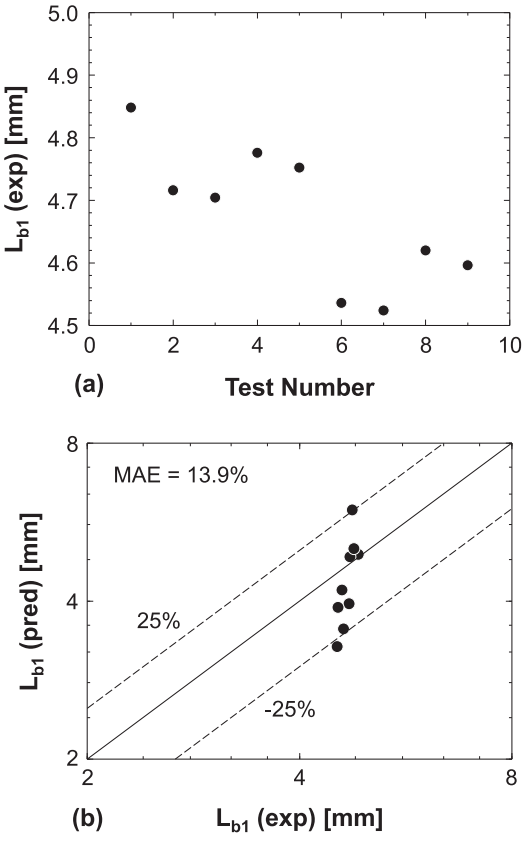

Fig. 9. (a) Measured bubble length in upstream unit cell. (b) Comparison of measured bubble length in upstream unit cell with model predictions.

are predicted by the model with a mean absolute error (MAE) of 13.9%, where

$$\mathrm{MAE} = \frac{1}{N}\sum \frac{|L_{b1,pred} - L_{b1,exp}|}{L_{b1,exp}} \times 100\%. \quad (39)$$

Shown in Fig. 10(a) are experimental data of initial slug length at the location of slug flow initiation, which vary from 1 to 3 mm. Fig. 10(b) shows that measured initial slug length data are predicted by the model with a MAE of 12.6%. This demonstrates the effectiveness of the new instability model discussed earlier in predicting initial slug flow parameters.

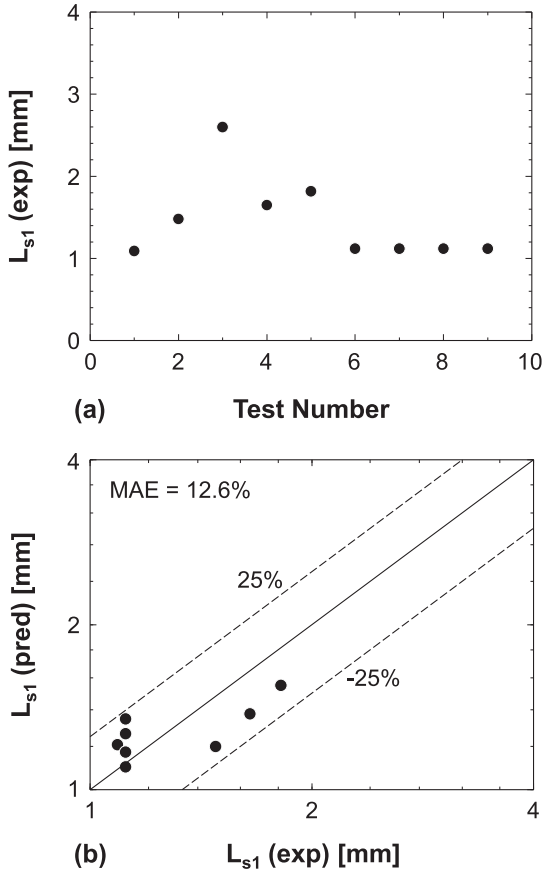

Fig. 10. (a) Measured slug length in upstream unit cell. (b) Comparison of measured slug length in upstream unit cell with model predictions.

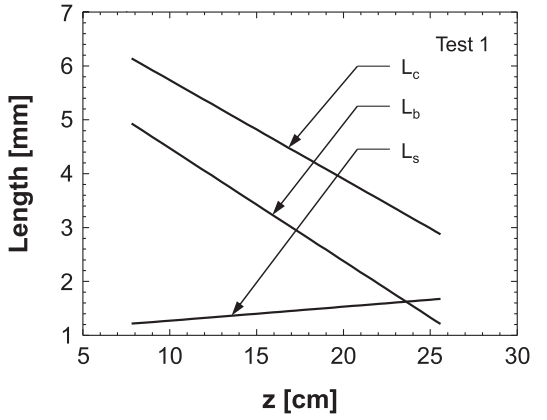

Fig. 11. Predicted axial variations of bubble length, liquid slug length, and unit cell length for Test 1.

Predicted axial variations of the slug and bubble lengths are found to follow similar trends for all nine tests. Fig. 11 shows variations of bubble, slug, and unit cell lengths along the microchannel for Test 1. Due to condensation, bubble length is shown decreasing appreciably, while the slug length increases slightly. Differences in slopes between the two is attributed to much smaller homogenous density around the bubble compared to liquid slug density. Fig. 11 also shows the cell length decreases appreciably along the channel, albeit more slowly than the bubble length.

Fig. 12(a) shows the measured total pressure drop for all nine tests. Clearly, pressure drop is dictated mostly by mass velocity, G, and decreases with decreasing G. Fig. 12(b) shows good agreement between measured total pressure drop and predictions using the universal approach by Kim and Mudawar [40], evidenced by a MAE of 13.0%. This proves that the universal approach is very effective for slug flow predictions.

Recall that slug flow consists of several unit cells having different lengths, with each unit cell consisting of a single vapor bubble and a single liquid slug. As indicated by Eqs. (37) and (38), constant heat transfer coefficient values are assumed for the bubble and slug regions, respectively, of the unit cell. Eq. (34) proves that the average heat transfer coefficient, h, is dictated by the bubble and slug lengths. Fig. 13(a) shows axial variations of the experimentally determined heat transfer coefficient, h, for all nine tests. Notice the gradual, albeit slow, decline of h with z, which can be attributed mostly to the axially decreasing bubble length (see Fig. 11), where the heat transfer coefficient is highest within a unit cell. Fig. 13(b) shows very good agreement between the measured average heat transfer coefficient and predictions of the present heat transfer model, evidenced by a MAE of 10.2% Fig. 14 shows the predicted h along the axial direction for Test 1, indicating that

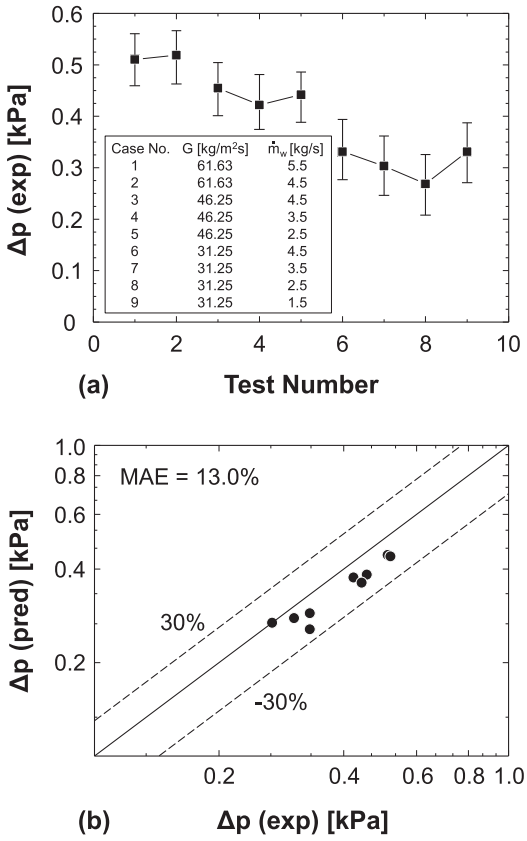

Fig. 12. (a) Measured total pressure drop. (b) Comparison of measured pressure drop with predictions of the universal approach.

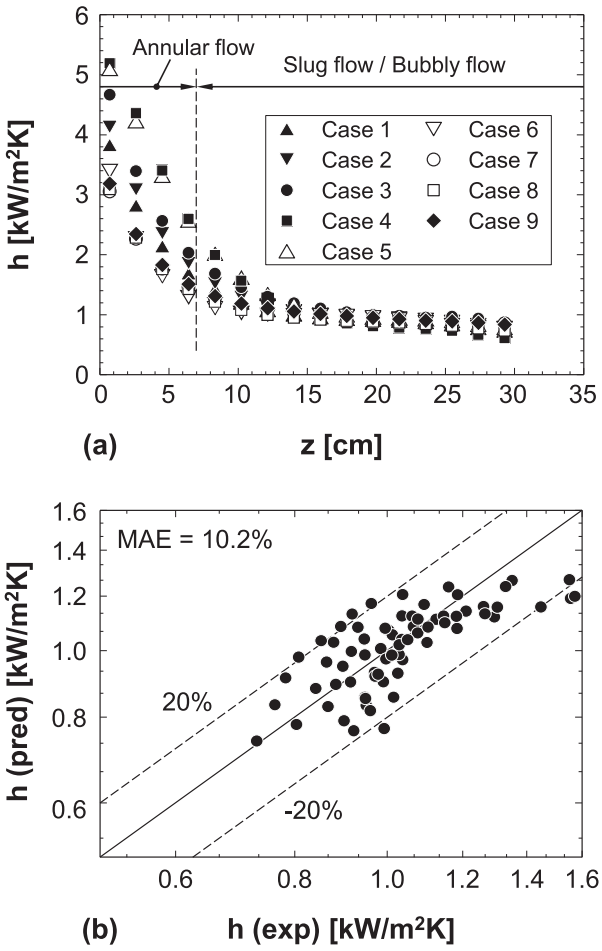

Fig. 13. (a) Measured axial variations of heat transfer coefficient. (b) Comparison of measured heat transfer coefficient with model predictions.

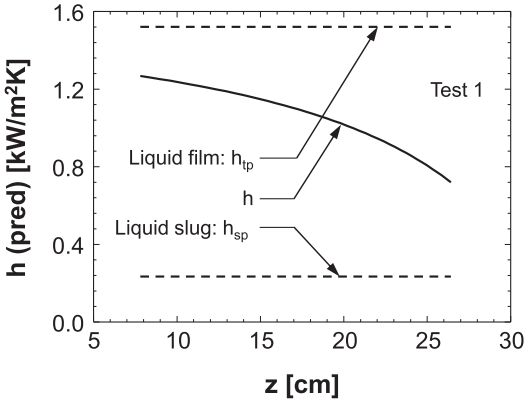

Fig. 14. Axial variation of heat transfer coefficient for Test 1.

it decreases monotonously due to the fact that bubble length decreases but slug length increases along the stream-wise direction, where the two-phase heat transfer coefficient around vapor bubbles is much higher than the single phase heat transfer coefficient in liquid slugs.

The present model is based on the assumption that values of the heat transfer coefficients associated with the bubble and slug in downstream unit cells are dictated mostly by corresponding values in the most upstream unit cell. Therefore, as discussed in the previous paragraph, axial variations in the average heat transfer

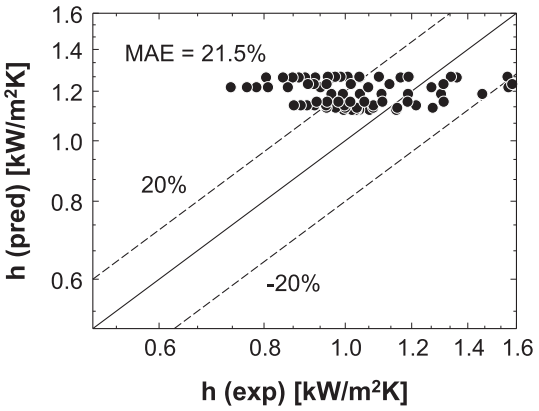

Fig. 15. Comparison of measured heat transfer coefficient data with predictions assuming constant heat transfer coefficient, proving the need to incorporate axial changes of bubble and slug lengths to achieving accurate heat transfer predictions.

coefficient are associated mostly with axial variations of bubble and slug lengths. This raises an important question concerning the use of a simplified model for heat transfer in slug flow based only on bubble and slug lengths of the most upstream unit cell, and which ignores axial length variations. In effect, this simplified approach uses bubble and slug parameters equivalent to those used in adiabatic slug flow [15–20], and which would predict a constant average heat transfer coefficient along the channel. Fig. 15 shows strong departure between the measured average heat transfer coefficient and predictions based on the simplified approach. This proves that incorporating the axial variations of bubble and slug lengths resulting from condensation is essential to achieving accurate heat transfer predictions.

7. Conclusions

This study investigated the problem of slug flow condensation of FC-72 in micro-channels. Flow visualization experiments were performed to capture a series of unit cells, each comprised of a liquid slug and an elongated bubble, and to measure the axial extent of both. Also measured were pressure drop and temperature variations along the condensation module. The temperature data were used to determine axial profiles for both heat flux and quality. New interfacial instability theory was also developed to capture transition from annular flow to slug flow and obtain analytical expressions for bubble and slug lengths for the most upstream unit cell. Also presented was a detailed model for axial variations of bubble, slug, and unit cell lengths, which were used to determine axial variations of the heat transfer coefficient. Additionally, pressure drop data were compared to predictions of a recent universal correlation for condensation in micro-channels. Key findings from the study are as follows.

1. Slug flow in micro-channels can be initiated farther upstream in the channels by employing low mass velocities. Unlike slug flow in macro channels, where small bubbles are entrained in the liquid slugs, no such bubbles were observed in the present micro-channel experiments.
2. Thermodynamic equilibrium quality is an accurate measure of vapor content, and therefore cannot be used directly to determine slug flow parameters. Instead, an alternative definition of quality – true quality – is devised, which shows good agreement with the data.
3. Slug flow initiation can be described and theoretically modeled by applying instability theory to the liquid film interface in the upstream annular flow regime.

4. In the most upstream unit cell, bubble length is nearly the same (4.5–4.9 mm) for all test cases, while liquid slug length varies from 1 to 3 mm. Condensation along the channels causes a monotonic decrease in both bubble and unit cell lengths, and an increase in liquid slug length. Combined with the instability analysis, the new model shows good predictions of the measured bubble and liquid slug lengths.
5. Pressure drop data for the nine test cases are accurately predicted by a recently proposed universal correlation for condensation in micro-channels.
6. Axial variations of bubble and slug lengths have a profound influence on the local heat transfer coefficient. A heat transfer model that accounts for the axial changes in the bubble and slug lengths as well as both single-phase and two-phase heat transfer shows good agreement with the experimental data.

Acknowledgements

Support of the National Natural Science Foundation of China (No. 51506023) and China Scholarship Council for this study is gratefully acknowledged.

Appendix A. Instability between confined vapor/liquid layers without heat transfer

Fig. 6(a) illustrates the fundamental model for instability between a vapor layer of velocity U_g and thickness H_g, and a liquid layer of velocity U_f and thickness H_f, which are confined between two infinite parallel solid walls. Gravity is neglected because of its insignificant influence in small channel flows. Shown is a 2D coordinate system centered in the y-direction along the unperturbed interface between the two layers. Disturbances to the system induce interfacial perturbations, which are de-stabilized by inertial forces against the stabilizing effects of surface tension. The solution to the instability problem is initiated by defining a velocity potential of the form $\phi_k = \phi_k(z, y, t)$ for each of the vapor and liquid layers (k = g for vapor and f for liquid), for which $(\vec{u}_k, \vec{v}_k) = \nabla\phi_k$.

Continuity for the individual layers gives

$$\frac{\partial u_g}{\partial z} + \frac{\partial v_g}{\partial y} = \frac{\partial^2 \phi_g}{\partial z^2} + \frac{\partial^2 \phi_g}{\partial y^2} = 0 \tag{A1a}$$

and

$$\frac{\partial u_f}{\partial z} + \frac{\partial v_f}{\partial y} = \frac{\partial^2 \phi_f}{\partial z^2} + \frac{\partial^2 \phi_f}{\partial y^2} = 0. \tag{A1b}$$

The potential solution must satisfy the conditions of zero velocity perpendicular to the solid walls,

$$v_g = \frac{\partial \phi_g}{\partial y} = 0 \text{ at } y = H_g, \tag{A2a}$$

and

$$v_f = \frac{\partial \phi_f}{\partial y} = 0 \text{ at } y = -H_f. \tag{A2b}$$

The interface is assumed to undergo disturbances of the form

$$\eta(z,t) = \eta_0 \exp[ik(z - ct)], \tag{A3}$$

where k and c are the wave number and wave speed, respectively; the latter can acquire both real and imaginary components. Eqs. (A1a) and (A1b) and the boundary conditions given by Eqs. (A2a) and (A2b) are satisfied by the following forms of the potential functions,

$$\phi_g = A_g \cosh[k(y - H_g)] \exp[ik(z - ct)] \tag{A4a}$$

and

$$\phi_f = A_f \cosh[k(y + H_f)] \exp[ik(z - ct)]. \tag{A4b}$$

The individual layers must satisfy the following kinematic boundary conditions at the interface (y = 0),

$$\frac{D\eta}{Dt} = \frac{\partial \eta}{\partial t} + U_g \frac{\partial \eta}{\partial z} = v_g = \frac{\partial \phi_g}{\partial y} \tag{A5a}$$

and

$$\frac{D\eta}{Dt} = \frac{\partial \eta}{\partial t} + U_f \frac{\partial \eta}{\partial z} = v_f = \frac{\partial \phi_f}{\partial y}. \tag{A5b}$$

Eqs. (A5a) and (A5b) are used to derive relations for coefficients A_g and A_f of Eqs. (A4a) and (A4b), respectively, in terms of η_0,

$$A_g = i\eta_0 (U_g - c)/\sinh(-kH_g), \tag{A6a}$$

and

$$A_f = i\eta_0 (U_f - c)/\sinh(kH_f). \tag{A6b}$$

Another boundary condition for the interface is associated with normal stress balance,

$$p_g - p_f = \sigma \left\{ \left[1 + \left(\frac{\partial \eta}{\partial z} \right)^2 \right]^{3/2} \Big/ \frac{\partial^2 \eta}{\partial z^2} \right\}^{-1} \simeq \sigma \frac{\partial^2 \eta}{\partial z^2}. \tag{A7}$$

The equations of motion for the individual phases,

$$\rho_g \frac{Du_g}{Dt} = -\nabla p_g \tag{A8a}$$

and

$$\rho_f \frac{Du_f}{Dt} = -\nabla p_f, \tag{A8b}$$

yield the following respective relations for u_g and u_f,

$$\rho_g \left(\frac{\partial u_g}{\partial t} + U_g \frac{\partial u_g}{\partial z} \right) = \rho_g \left(\frac{\partial^2 \phi_g}{\partial t \partial z} + U_g \frac{\partial^2 \phi_g}{\partial z^2} \right) = -\frac{\partial p_g}{\partial z} \tag{A9a}$$

and

$$\rho_f \left(\frac{\partial u_f}{\partial t} + U_f \frac{\partial u_f}{\partial z} \right) = \rho_f \left(\frac{\partial^2 \phi_f}{\partial t \partial z} + U_f \frac{\partial^2 \phi_f}{\partial z^2} \right) = -\frac{\partial p_f}{\partial z}, \tag{A9b}$$

which can be differentiated relative to z to yield

$$\rho_g \left\{ \frac{\partial}{\partial t} \left(\frac{\partial^2 \phi_g}{\partial z^2} \right) + U_g \frac{\partial}{\partial z} \left(\frac{\partial^2 \phi_g}{\partial z^2} \right) \right\} = -\frac{\partial^2 p_g}{\partial z^2} \tag{A10a}$$

and

$$\rho_f \left\{ \frac{\partial}{\partial t} \left(\frac{\partial^2 \phi_f}{\partial z^2} \right) + U_f \frac{\partial}{\partial z} \left(\frac{\partial^2 \phi_f}{\partial z^2} \right) \right\} = -\frac{\partial^2 p_f}{\partial z^2}. \tag{A10b}$$

Introducing continuity Eq. (A1a) into (A10a) and (A1b) into (A10b) gives, respectively,

$$\rho_g \left(\frac{\partial^3 \phi_g}{\partial t \partial y^2} + U_g \frac{\partial^3 \phi_g}{\partial z\, \partial y^2} \right) = \frac{\partial^2 p_g}{\partial z^2} \tag{A11a}$$

and

$$\rho_f \left(\frac{\partial^3 \phi_f}{\partial t\, \partial y^2} + U_f \frac{\partial^3 \phi_f}{\partial z\, \partial y^2} \right) = \frac{\partial^2 p_f}{\partial z^2}. \tag{A11b}$$

Combining Eqs. (A11a) and (A11b) with the normal stress balance, Eq. (A7), differentiated twice relative to z, gives

$$\rho_g\left(\frac{\partial^3\phi_g}{\partial t\,\partial y^2}+U_g\frac{\partial^3\phi_g}{\partial z\,\partial y^2}\right)-\rho_f\left(\frac{\partial^3\phi_f}{\partial t\,\partial y^2}+U_f\frac{\partial^3\phi_f}{\partial z\,\partial y^2}\right)=\sigma\frac{\partial^4\eta}{\partial z^4}. \tag{A12}$$

Solving Eq. (A12) and setting $y = 0$ give

$$\rho_g A_g\,(U_g-c)\,i\,\cosh(kH_g)-\rho_f A_f\,(U_f-c)\,i\,\cosh(kH_f)=\sigma\eta_0 k. \tag{A13}$$

Now, substituting Eqs. (A6a) and (A6b) into Eq. (A13) gives

$$\rho_g^+(U_g-c)^2+\rho_f^+(U_f-c)^2=\sigma k, \tag{A14}$$

where $\rho_g^+=\rho_g\coth(kH_g)$ and $\rho_f^+=\rho_f\coth(kH_f)$. For an unstable interface, the solution to quadratic Eq. (A14) can be presented as

$$c=c_r+ic_i, \tag{A15}$$

where

$$c_r=\frac{\rho_g^+U_g+\rho_f^+U_f}{\rho_g^++\rho_f^+}, \tag{A16a}$$

and

$$c_i=\left[\frac{\rho_g^+\rho_f^+(U_g-U_f)^2}{(\rho_g^++\rho_f^+)^2}-\frac{\sigma k}{(\rho_g^++\rho_f^+)}\right]^{1/2}. \tag{A16b}$$

In the above equations, c_r represents the wave propagation speed of the interfacial disturbances, and c_i provides a measure of temporal growth of amplitude of the unstable interface. Setting $c_i = 0$ gives a relation for the critical wave number, k_c, and corresponding critical wavelength, λ_c ($=2\pi/k_c$), corresponding to the onset of instability.

References

[1] T.M. Anderson, I. Mudawar, Microelectronic cooling by enhanced pool boiling of a dielectric fluorocarbon liquid, J. Heat Transfer – Trans. ASME 111 (1989) 752–759.
[2] I. Mudawar, Two-phase micro-channel heat sinks: theory, applications and limitations, J. Electron. Packag. – Trans. ASME 133 (2011), 041002-2.
[3] J. Lee, I. Mudawar, Fluid flow and heat transfer characteristics of low temperature two-phase micro-channel heat sinks – Part 1: experimental methods and flow visualization results, Int. J. Heat Mass Transfer 51 (2008) 4315–4326.
[4] M.K. Sung, I. Mudawar, Single-phase and two-phase heat transfer characteristics of low temperature hybrid micro-channel/micro-jet impingement cooling module, Int. J. Heat Mass Transfer 51 (2008) 3882–3895.
[5] W. Qu, I. Mudawar, S.-Y. Lee, S.T. Wereley, Experimental and computational investigation of flow development and pressure drop in a rectangular micro-channel, J. Electron. Packag. – Trans. ASME 128 (2006) 1–9.
[6] S.M. Kim, J. Kim, I. Mudawar, Flow condensation in parallel rectangular micro-channels – Part 1: experimental results and assessment of pressure drop correlations, Int. J. Heat Mass Transfer 55 (2012) 971–983.
[7] S.M. Kim, I. Mudawar, Flow condensation in parallel rectangular micro-channels – Part 2: heat transfer results and correlation technique, Int. J. Heat Mass Transfer 55 (2012) 984–994.
[8] S.M. Kim, I. Mudawar, Theoretical model for annular flow condensation in rectangular micro-channels, Int. J. Heat Mass Transfer 55 (2012) 958–970.
[9] R.W. Lockhart, R.C. Martinelli, Proposed correlation of data for isothermal two-phase, two-component flow in pipes, Chem. Eng. Prog. 45 (1949) 39–48.
[10] M.M. Shah, An improved and extended general correlation for heat transfer during condensation in plain tubes, HVAC&R Res. 15 (2009) 889–913.
[11] M. Zhang, R.L. Webb, Correlation of two-phase friction for refrigerants in small-diameter tubes, Exp. Therm. Fluid Sci. 25 (2001) 131–139.
[12] W.-W.W. Wang, T.D. Radcliff, R.N. Christensen, A condensation heat transfer correlation for millimeter-scale tubing with flow regime transition, Exp. Therm. Fluid Sci. 26 (2002) 473–485.
[13] T. Zhang, B. Cao, Y. Fan, Y. Gonthier, L. Luo, S. Wang, Gas-liquid flow in circular microchannel. Part I: Influence of liquid physical properties and channel diameter on flow patterns, Chem. Eng. Sci. 66 (2011) 5791–5803.
[14] A. Odaymet, H. Louahlia-Gualous, Experimental study of slug flow for condensation in a single square microchannel, Exp. Therm. Fluid Sci. 38 (2012) 1–13.
[15] A.E. Dukler, M.G. Hubbard, A model for gas-liquid slug flow in horizontal and near-horizontal tubes, Ind. Eng. Chem. Fundam. 14 (1975) 337–347.
[16] M.K. Nicholson, K. Aziz, G.A. Gregory, Intermittent two phase flow in horizontal pipes: predictive models, Can. J. Chem. Eng. 56 (1978) 653–663.
[17] T. Fukano, A. Kariyasaki, M. Kagawa, Flow patterns and pressure drop in isothermal gas-liquid concurrent flow in a horizontal capillary tube, in: Proc. National Heat Transfer Conf., vol. 4, Philadelphia, PA, 1989, pp. 153–161.
[18] M. Suo, P. Griffith, Two-phase flow in capillary tubes, J. Basic Eng. 86 (1964) 576–582.
[19] Y. Taitel, D. Barnea, Two-phase slug flow, Adv. Heat Transfer 20 (1990) 83–132.
[20] P.M.-Y. Chung, M. Kawaji, The effect of channel diameter on adiabatic two-phase flow characteristics in microchannels, Int. J. Multiphase Flow 30 (2004) 735–761.
[21] S. Levy, Forced convection subcooled boiling-prediction of vapor volumetric fraction, Int. J. Heat Mass Transfer 10 (1967) 951–965.
[22] N. Zuber, M. Tribus, J.W. Westwater, The hydrodynamic crisis in pool boiling of saturated and subcooled liquids, in: Int. Dev. Heat Transfer: Proc. 1961–62 Int. Heat Transfer Conf., Boulder, CO, 1961, pp. 230–236.
[23] I. Mudawar, A.H. Howard, C.O. Gersey, An analytical model for near-saturated pool boiling CHF on vertical surfaces, Int. J. Heat Mass Transfer 40 (1997) 2327–2339.
[24] C.O. Gersey, I. Mudawar, Effects of heater length and orientation on the trigger mechanism for near-saturated flow boiling critical heat flux – I. Photographic study and statistical characterization of the near-wall interfacial features, Int. J. Heat Mass Transfer 38 (1995) 629–641.
[25] C.O. Gersey, I. Mudawar, Effects of heater length and orientation on the trigger mechanism for near-saturated flow boiling critical heat flux – II. Critical heat flux model, Int. J. Heat Mass Transfer 38 (1995) 643–654.
[26] J.C. Sturgis, I. Mudawar, Critical heat flux in a long, rectangular channel subjected to onesided heating – I. Flow visualization, Int. J. Heat Mass Transfer 42 (1999) 1835–1847.
[27] J.C. Sturgis, I. Mudawar, Critical heat flux in a long, rectangular channel subjected to onesided heating – II. Analysis of critical heat flux data, Int. J. Heat Mass Transfer 42 (1999) 1849–1862.
[28] P.Y. Lin, T.J. Hanratty, Prediction of the initiation of slug with linear stability theory, Int. J. Multiphase Flow 12 (1986) 77–98.
[29] E.T. Hurlburt, T.J. Hanratty, Prediction of the transition from stratified to slug and plug flow for long pipes, Int. J. Multiphase Flow 28 (2002) 707–729.
[30] A. Sanchis, G.W. Johnson, A. Jensen, The formation of hydrodynamic slugs by the interaction of waves in gas-liquid two-phase pipe flow, Int. J. Multiphase Flow 37 (2011) 358–368.
[31] H. Lamb, Hydrodynamics, sixth ed., Dover, New York, 1945.
[32] L.M. Milne-Thompson, Theoretical Hydrodynamics, fourth ed., Macmillan, New York, 1960.
[33] J. Ratulowski, H.-C. Chang, Transport of gas bubbles in capillaries, Phys. Fluids 1 (1989) 1642–1655.
[34] T. Thulasidas, M. Abraham, R. Cerro, Bubble-train flow in capillaries of circular and square cross section, Chem. Eng. Sci. 50 (1995) 183–199.
[35] W.B. Kolb, R.L. Cerro, The motion of long bubbles in tubes of square cross section, Phys. Fluids 5 (1993) 1549–1557.
[36] W.B. Kolb, R.L. Cerro, Coating the inside of a capillary of square cross section, Chem. Eng. Sci. 46 (1991) 2181–2195.
[37] S. Zivi, Estimation of steady-state steam void-fraction by means of the principle of minimum entropy production, J. Heat Transfer – Trans. ASME 86 (1964) 247–251.
[38] M.T. Kreutzer, F. Kapteijn, J.A. Moulijn, J.J. Heiszwolf, Multiphase monolith reactors: chemical reaction engineering of segmented flow in microchannels, Chem. Eng. Sci. 60 (2005) 5895–5916.
[39] Y. Han, N. Shikazono, Measurement of liquid film thickness in micro square channel, Int. J. Multiphase Flow 35 (2009) 896–903.
[40] S.M. Kim, I. Mudawar, Universal approach to predicting two-phase frictional pressure drop for adiabatic and condensing mini/micro-channel flows, Int. J. Heat Mass Transfer 55 (2012) 3246–3261.
[41] A.M. Jacobi, J.R. Thome, Heat transfer model for evaporation of elongated bubble flows in microchannels, J. Heat Transfer – Trans. ASME 124 (2002) 1131–1136.
[42] R.K. Shah, A.L. London, Laminar Flow Forced Convection in Ducts: A Source Book for Compact Heat Exchanger Analytical Data, Academic Press, New York, 1978.